

# Switching the sign of the Casimir force between two PEMC spheres

Tanja Schoger<sup>1</sup> and Gert-Ludwig Ingold<sup>1</sup>

<sup>1</sup>*Institut für Physik, Universität Augsburg, 86135 Augsburg, Germany*

For non-reciprocal objects in vacuum, the Casimir interaction can become repulsive. Here, we present a comprehensive study for idealized non-reciprocal materials known as perfect electromagnetic conductors (PEMC). The system consists of two spheres made of different PEMC materials, including the plane-sphere geometry as a particular case. The sign of the Casimir force does not only depend on the distance between the spheres and their geometric parameters but can be controlled by adjusting the temperature. A repulsive Casimir interaction at small distances allows for stable equilibrium configurations of the spheres. A sum rule previously derived for the plane-plane geometry at zero temperature is violated in general, if at least one plane is replaced by a sphere.

## I. INTRODUCTION

Quantum and thermal fluctuations of the electromagnetic field can dominate the interaction of neutral objects at the nano-scale through the Casimir effect. Typically, the associated force is attractive and at submicron distances becomes strong enough to be relevant for micro- and nano-electromechanical systems. Resulting phenomena like stiction can then affect the functionality of such devices [1]. The possibility to switch from attractive to repulsive Casimir interaction through an external control parameter like the temperature is therefore of great interest. Furthermore, if the Casimir force changes its sign from repulsive to attractive with increasing distance between the objects, a stable equilibrium configuration exists.

Casimir repulsion was already studied and experimentally realized in various systems. For dielectric objects of relative permittivity  $\epsilon_1$  and  $\epsilon_2$  immersed in a liquid of permittivity  $\epsilon_3$ , it has been known for a long time that repulsion can occur provided  $\epsilon_1(i\xi) > \epsilon_3(i\xi) > \epsilon_2(i\xi)$  at imaginary frequencies  $\xi$  [2]. More recently, repulsion in such a setup was demonstrated experimentally [3].

A repulsive Casimir force can also be realized without a medium between objects. Already Boyer [4] pointed out that a perfect electric conductor and a perfect magnetic conductor repel each other. Since then various systems have been studied where repulsion can occur, involving metamaterials [5, 6], topological insulators [7–12], Weyl semimetals [13, 14] or magnetoelectric materials [15, 16] to name but a few.

In 2018, Rode *et al.* [17] generalized the system considered by Boyer by studying the Casimir interaction between so-called perfect electromagnetic conductor (PEMC) plates at zero temperature. PEMC materials interpolate between a perfect electric and magnetic conductor [18]. They are a special kind of non-reciprocal medium which can be obtained as a limit from a broader class of polarization-mixing materials, the so-called biisotropic materials [19].

Theoretical studies of objects embedded in a medium fulfilling the condition mentioned above revealed the existence of a stable equilibrium position which depends on the size of the objects as well as on temperature [20, 21].

In the present paper, we extend this approach to non-reciprocal materials in vacuum, for which, except for a study within the pairwise summation approximation [9], only planar geometries have been examined so far. Specifically, we will analyze the Casimir force for two dissimilar PEMC spheres for arbitrary radii and distances. Of particular interest is the influence of thermal fluctuations, since the temperature can serve as an external control parameter. The sphere-plane geometry will be included in our analysis as a limiting case.

In the following, we will provide analytical and numerical results for the Casimir interaction between two dissimilar PEMC spheres to cover the full range of parameters. Our numerical results are based on a plane-wave description introduced earlier for dielectric spherical objects [22]. For the present work, we adapted this approach to include biisotropic materials.

This paper is organized as follows. In Sec. II, we describe the scattering of electromagnetic waves at a single biisotropic sphere including the limiting case of a sphere consisting of a PEMC material. Section III continues with a brief introduction to the scattering approach to the Casimir interaction and its application to spherical objects. Next, we apply the scattering formalism to calculate the Casimir interaction for short (Sec. IV) and large separations (Sec. V) between the PEMC spheres. Additional analytical results for the Casimir interaction are obtained for high temperatures in Sec. VI. In Sec. VII, we examine whether a sum rule for the Casimir force derived for the plane-plane geometry [17] carries over to the sphere-sphere setup. Section VIII discusses the Casimir force over the whole range of distances, temperatures, and geometrical parameters. We investigate the conditions for which temperature can serve as a control parameter to switch from attraction to repulsion as well as the conditions for stable equilibrium positions. Concluding remarks are given in Sec. IX and the Appendix contains some definitions and technical details.

## II. SCATTERING AT A PEMC SPHERE

The reflection operator at a single sphere is the main ingredient for the scattering approach to the Casimir in-

teraction which we will discuss in the next section. We can profit from previous work [23] by starting with a biisotropic model from which PEMC can be obtained as a limiting case.

The constitutive equations for a biisotropic material in the frequency domain are given by

$$\begin{pmatrix} \mathbf{D} \\ \mathbf{B} \end{pmatrix} = \begin{pmatrix} \epsilon & \alpha \\ \beta & \mu \end{pmatrix} \begin{pmatrix} \mathbf{E} \\ \mathbf{H} \end{pmatrix} \quad (1)$$

with the permittivity  $\epsilon$  and the permeability  $\mu$ . The biisotropy parameters  $\alpha$  and  $\beta$  account for the magneto-to-electric and electro-to-magnetic coupling, respectively. All four parameters are scalar functions of the frequency. If the Onsager reciprocal relation  $\alpha = -\beta^*$  is violated, the material is non-reciprocal (see e.g. [24] for a review). The constitutive equations above are, for example, used to describe topological insulators (see e.g. [25] for a review).

The reflection operator  $\mathcal{R}$  of a spherical object is usually expressed in a spherical-wave basis  $|\ell, m, P, s\rangle$ . Each multipole mode is defined by its angular momentum  $\ell = 1, 2, \dots$  with  $m = -\ell, \dots, 0, \dots, \ell$ , the polarization  $P$ , which is either electric (E) or magnetic (M) and a parameter  $s$  which describes an incoming (reg) or outgoing (out) wave with respect to the sphere center. Within the  $2 \times 2$ -dimensional polarization subspace of the spherical-wave basis, the matrix elements of the reflection operator for a biisotropic sphere can be expressed as

$$\langle P | \mathcal{R} | P' \rangle = -i^{P' - P} (\mathbf{R})_{P, P'}, \quad (2)$$

where we associate  $P = 1$  ( $P = 2$ ) to E (M) polarized modes and the matrix  $\mathbf{R}$  contains the Mie coefficients which for biisotropic materials were derived in [23]. As the constitutive equations used there differ from (1) and we consider imaginary frequencies instead of real frequencies, we provide explicit expressions for the Mie coefficients in Appendix A.

By choosing the material parameters in the constitutive equation (1) as

$$\alpha = \beta = q, \quad \epsilon = q \cot(\theta), \quad \mu = q \tan(\theta), \quad (3)$$

one obtains PEMC by taking the limit  $q \rightarrow \infty$ . This class of materials is parametrized by the angle  $\theta$  taking values between 0 and  $\pi/2$ . The two boundary cases correspond to the perfect electric (PEC) and perfect magnetic (PMC) conductor, respectively [19]. According to the choice of  $\alpha$  and  $\beta$  in (3), PEMC are non-reciprocal.

It can be shown that the reflection matrix in (2) for a PEMC sphere can be expressed as

$$\mathbf{R}_{\text{PEMC}} = \mathbf{D} \mathbf{R}_{\text{PEC}} \mathbf{D}^{-1}, \quad (4)$$

where  $\mathbf{R}_{\text{PEC}}$  is the reflection matrix for a perfect electric conductor while the duality transformation matrix

$$\mathbf{D} = \begin{pmatrix} \cos(\theta) & \sin(\theta) \\ -\sin(\theta) & \cos(\theta) \end{pmatrix} \quad (5)$$

depends on the material parameter  $\theta$  [26]. Explicit expressions are given in (A12)–(A14).

Clearly, PEMC constitute an idealization of real non-reciprocal materials. For a theoretical study, however, they allow to characterize the material properties of the system by the single parameter  $\theta$ . We can thus analyze the interplay between geometry, temperature and material properties of the system. Furthermore, they may provide a guiding line for future experiments aiming at realizing Casimir repulsion by making use of non-reciprocal materials. Moreover, the PEMC model allows us to derive analytical results for the Casimir interaction, as can be seen in the following sections.

### III. SCATTERING APPROACH TO THE CASIMIR INTERACTION

The scattering approach to the Casimir effect was originally developed for objects consisting of reciprocal materials [27, 28]. A recent general study confirmed that in thermal equilibrium, the scattering approach holds even for non-reciprocal objects [29]. For two non-reciprocal plates, this was already shown in [12].

In our calculations, we will evaluate as the primary quantity the Casimir free energy  $\mathcal{F}$  from which the Casimir force  $F$  can be obtained by taking the derivative with respect to the surface-to-surface distance  $L$  between the objects according to

$$F = -\frac{\partial \mathcal{F}}{\partial L}. \quad (6)$$

At finite temperatures, the Casimir free energy can be expressed as a sum over Matsubara frequencies  $\xi_n = 2\pi k_B T n / \hbar$

$$\mathcal{F} = \frac{k_B T}{2} \sum_{n=-\infty}^{\infty} f_{|n|} \quad (7)$$

with

$$f_n = \log \det(1 - \mathcal{M}(i\xi_n)) = -\sum_{r=1}^{\infty} \frac{\text{tr} \mathcal{M}^r(i\xi_n)}{r}. \quad (8)$$

The round-trip operator

$$\mathcal{M} = \mathcal{T}_{12} \mathcal{R}_2 \mathcal{T}_{21} \mathcal{R}_1 \quad (9)$$

describes the scattering process of the electromagnetic field between the two objects. The operator  $\mathcal{R}$  accounts for the reflection at an object and the operator  $\mathcal{T}$  translates the electromagnetic field from the reference frame of one object to the other (see Fig. 1).

In the second equality in (8) we made use of Jacobi's formula and the Mercator series. The summation index  $r$  accounts for the number of round-trips of the electromagnetic field between the two objects. The single-round-trip contribution is thus obtained by retaining only the term

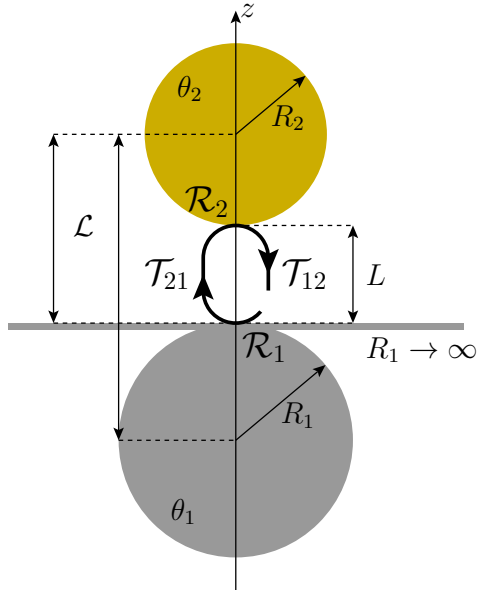


FIG. 1. Scattering geometry consisting of two spheres or, in the limit  $R_1 \rightarrow \infty$ , a sphere in front of a plane placed along the  $z$ -axis with a surface-to-surface distance  $L$ . In the sphere-sphere geometry, we also define the distance  $\mathcal{L} = L + R_1 + R_2$  and for the sphere-plane setup we will use  $\mathcal{L} = L + R_2$ . The objects are made of PEMC with parameters  $\theta_1$  and  $\theta_2$ . The round-trip operator (9) is indicated by the black loop in the gap.

with  $r = 1$ . While the round-trip expansion is particularly useful to derive analytical results, numerical approaches are usually based on evaluating the determinant in (8).

At zero temperature, the Matsubara sum turns into an integral over imaginary frequencies  $\omega = i\xi$ . In the opposite limit of high temperatures, the free energy

$$\mathcal{F}_T = \frac{k_B T}{2} f_0 \quad (10)$$

depends exclusively on the contribution of the Matsubara frequency  $\xi_0$ . This expression is proportional to the temperature and of purely entropic origin.

In order to calculate the Casimir free energy, we evaluate the trace in (8) in an appropriate basis set, depending on the geometry of the scattering problem. We will specifically consider the setup depicted in Fig. 1 consisting of two spherical particles with radii  $R_1$  and  $R_2$  at a surface-to-surface distance  $L$  and made of PEMC with parameters  $\theta_1$  and  $\theta_2$ . The sphere centers are located on the  $z$ -axis and serve as origins of the reference frames in which the reflection of electromagnetic waves is described. Their distance is given by  $\mathcal{L} = L + R_1 + R_2$ . We will later make use of the aspect ratio

$$x = \frac{L}{R_{\text{eff}}} \quad (11)$$

with the effective radius

$$R_{\text{eff}} = \frac{R_1 R_2}{R_1 + R_2}. \quad (12)$$

In the limit  $R_1 \rightarrow \infty$ , the sphere-sphere geometry turns into the sphere-plane geometry. The transition from equally sized spheres to a sphere in front of a plane can be described by the dimensionless parameter

$$u = \frac{R_1 R_2}{(R_1 + R_2)^2} \quad (13)$$

which takes values between 0 in the case of the sphere-plane geometry and 1/4 for two spheres of equal radii.

While the reflection operator matrix elements are conveniently expressed in the spherical-wave basis introduced in Sec. II, a plane-wave description is better suited for the translation operator. For the plane-wave basis, we employ the angular spectral representation [30]. Omitting the imaginary frequency  $\xi$ , which is constant during the whole round-trip, we denote the basis by  $|\mathbf{k}, p, \pm\rangle$ , where  $\mathbf{k} = k(\cos(\varphi), \sin(\varphi))$  is the transversal part of the wave vector  $\mathbf{K}$ . The dispersion relation can then be expressed as  $\xi^2 = c^2(\mathbf{k}^2 - \kappa^2)$ , where  $\kappa$  is the imaginary wave vector component in  $z$ -direction. The polarization  $p$  of the plane wave is defined with respect to a plane perpendicular to the  $z$ -axis and can be transverse magnetic (TM) or transverse electric (TE). The signs  $\pm$  refer to the direction of propagation along the  $z$ -axis. Within the plane-wave basis, the translation operator is diagonal with the matrix elements

$$\langle \mathbf{k}, p, \pm | \mathcal{T} | \mathbf{k}', p', \pm \rangle = e^{-\kappa \mathcal{L}} \delta(\mathbf{k} - \mathbf{k}') \delta_{p,p'}. \quad (14)$$

The trace over the  $r$ -fold round-trip operator (8) in the plane-wave basis is thus given by [31]

$$\begin{aligned} \text{tr} \mathcal{M}^r = & \sum_{p_1, \dots, p_{2r}} \int \frac{d\mathbf{k}_1 \dots d\mathbf{k}_{2r}}{(2\pi)^{4r}} \prod_{j=1}^r e^{-\kappa_{2j} \mathcal{L}} e^{-\kappa_{2j-1} \mathcal{L}} \\ & \times \langle \mathbf{k}_{2j+1}, p_{2j+1}, - | \mathcal{R}_2 | \mathbf{k}_{2j}, p_{2j}, + \rangle \\ & \times \langle \mathbf{k}_{2j}, p_{2j}, + | \mathcal{R}_1 | \mathbf{k}_{2j-1}, p_{2j-1}, - \rangle, \end{aligned} \quad (15)$$

where cyclic indices  $2r + 1 \equiv 1$  are used to account for the trace.

Within the plane-wave basis, the reflection operator can be determined by means of a basis change

$$\langle p | \mathcal{R} | p' \rangle = \sum_{P, P' = E, M} \langle p | P \rangle \langle P | \mathcal{R} | P' \rangle \langle P' | p' \rangle \quad (16)$$

and making use of the reflection matrix elements in the spherical-wave basis discussed in Sec. II and Appendix A. For simplicity, we omitted in (16) all indices of the bases, except for the polarization. The basis transformation coefficients  $\langle p | P \rangle$  and  $\langle P | p \rangle$  can be found in [32]. Together

with (2) we thus obtain for a biisotropic sphere [33]

$$\langle \mathbf{k}, p | \mathcal{R} | \mathbf{k}', p' \rangle = \frac{2\pi c}{\xi \kappa} \left[ AS_{p,p'} + (-1)^{p+p'} BS_{\bar{p},\bar{p}'} \right. \\ \left. - (-1)^p CS_{\bar{p},p'} + (-1)^{p'} DS_{p,\bar{p}'} \right]. \quad (17)$$

In the notation above, we associate  $\bar{p}$  with the opposite polarization to  $p$  and we set  $p = 1$  ( $p = 2$ ) for TM (TE) polarized waves. The coefficients  $A$ ,  $B$ ,  $C$  and  $D$  account for the polarization transformations and are given in [31]. They depend on the incoming and outgoing wave vectors  $A = A(\mathbf{K}, \mathbf{K}')$ .  $S_{p,p'}$  are the elements of the amplitude scattering matrix [23] and are reproduced in (A15) for imaginary frequencies and our definitions of the reflections matrix elements.

As indicated in (10), the high-temperature limit of the Casimir free energy is determined by the zero-frequency contribution, for which the amplitude scattering matrix simplifies. The polarization changing coefficients  $B, C$  and  $D$  in (17) vanish in this limit, while  $A$  tends to one [31]. Furthermore, following the argument given in Appendix A, even in the plane-wave basis the leading order of the reflection coefficients for a PEMC sphere in the low-frequency limit are obtained by a duality transformation

$$\langle p | \mathcal{R} | p' \rangle = \frac{2\pi c}{\xi k} (\mathbf{D} \mathbf{S}_{\text{PEC}} \mathbf{D}^{-1})_{p,p'}. \quad (18)$$

Here,  $\mathbf{S}_{\text{PEC}}$  defines the amplitude scattering matrix for a perfect reflector in the low-frequency limit (A18). This simplification at very low frequencies will allow for analytical calculations of the Casimir interaction in the high-temperature regime.

#### IV. SHORT-DISTANCE ASYMPTOTICS

If the sphere radii are large compared to the surface-to-surface distance,  $R_1, R_2 \gg L$ , the Casimir force is commonly treated within the proximity-force approximation (PFA) [34]. This approximation treats the Casimir interaction between the spheres in close vicinity as the interaction between parallel plate segments. As demonstrated in [33], the PFA result for two PEMC spheres can be obtained from an asymptotic expansion of the reflection coefficients for large radii. The round-trip decomposition of the Matsubara frequency contributions (8) was found as

$$f_{n,\text{PFA}} = -R_{\text{eff}} \int \frac{d\mathbf{k}}{2\pi\kappa} \text{Re} [\text{Li}_2(e^{2i\delta-2\kappa L})], \quad (19)$$

where  $\text{Li}_n(z)$  is the polylogarithm of order  $n$ .

The integral over  $\mathbf{k}$  can be calculated explicitly and yields

$$f_{n,\text{PFA}} = -\frac{1}{2x} \text{Re} [\text{Li}_3(e^{2i\delta-2n\tau})], \quad (20)$$

where  $x$  is the aspect ratio defined in (11) and  $\tau = 2\pi L/\lambda_T$  is a dimensionless temperature with the thermal wavelength  $\lambda_T = \hbar c/k_B T$ . The coefficients (20) and, as a consequence, the Casimir energy depend only on the difference of the PEMC parameters  $\theta_{1,2}$  of the two spheres

$$\delta = |\theta_2 - \theta_1|. \quad (21)$$

The limiting values  $\delta = 0$  and  $\pi/2$  correspond to two identical PEMC spheres and to a PEC and a PMC sphere, respectively. The nature of the Casimir force thus changes from attractive for two symmetric particles [35] to repulsive with increasing  $\delta$ .

In the zero-temperature limit, we already confirmed in [33] that our PFA result agrees with the one obtained by Rode et al. [17] and earlier ones [36, 37] obtained for a scalar field with pseudo-periodic boundary conditions

$$\mathcal{E}_{\text{PFA}} = -\frac{\hbar c}{720\pi L} \frac{1}{x} [\pi^4 - 30\delta^2(\pi - \delta)^2]. \quad (22)$$

This expression for the Casimir energy changes sign between  $\delta = 0$  and  $\pi/2$  and according to (6) the Casimir force changes sign as well. The critical value of  $\delta$  at which the force vanishes is given by

$$\delta_{\text{crit}}^{T=0} = \left( 1 - \sqrt{1 - 2\sqrt{\frac{2}{15}}} \right) \frac{\pi}{2} = 0.961 \dots \frac{\pi}{4}. \quad (23)$$

Here and in the following, it is convenient to express critical angles in units of the central angle  $\pi/4$  corresponding to a situation half-way between equal materials and a PEC-PMC setup.

The force thus changes its sign at  $\delta_{\text{crit}}$  and is attractive for systems with  $\delta < \delta_{\text{crit}}$  while being repulsive for  $\delta > \delta_{\text{crit}}$ . In the following, we are going to determine the temperature and distance corrections to the PFA result (22) and analyze how  $\delta_{\text{crit}}$  changes when we increase the temperature or the separation between the spheres.

##### A. Temperature corrections to PFA

We will now examine the temperature corrections to the critical angle introduced in (23). We thus consider the case  $L \ll \lambda_T \ll R_{\text{eff}}$  for  $\delta > 0$ , where the temperature corrections for  $\tau \ll 1$  can be calculated by applying the Mellin transform of the exponential in (20). After performing the sum over the Matsubara frequencies (7), we obtain

$$\mathcal{F}_{\text{PFA}} = -\frac{k_B T}{4x} \left[ \text{Re} [\text{Li}_3(e^{2i\delta})] + 2 \int_{c-i\infty}^{c+i\infty} \frac{ds}{2\pi i} \Gamma(s) \zeta(s) \text{Re} [\text{Li}_{s+3}(e^{2i\delta})] (2\tau)^{-s} \right], \quad (24)$$

where  $\Gamma(s)$  and  $\zeta(s)$  refer to the gamma function and the Riemann zeta function, respectively. The integration contour in the complex plane is chosen such that  $c > 1$ .

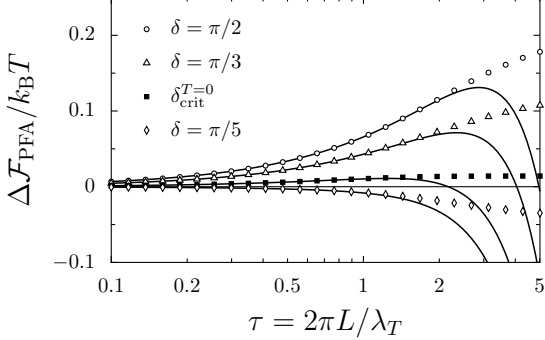


FIG. 2. Temperature corrections to the PFA result (22) for the Casimir energy in units of  $k_B T$  for various values of  $\delta$ . The symbols depict the numerically exact values and the solid lines represent the low-temperature expansion given in (25).

For  $\delta > 0$ , the integrand has single poles at  $s = 1, 0$  and  $-2n-1$  with  $n = 0, 1, 2, \dots$ . The pole at  $s = 1$  accounts for the zero-temperature result (22). The leading temperature corrections then arise from the poles at  $s = 0, -1$  and  $-3$ . Applying Cauchy's theorem and evaluating the residues, we find for the low-temperature expansion

$$\begin{aligned} \Delta\mathcal{F}_{\text{PFA}} &= \mathcal{F}_{\text{PFA}} - \mathcal{E}_{\text{PFA}} \\ &= -\frac{\hbar c}{720\pi L x} [5(\pi^2 - 6\delta(\pi - \delta))\tau^2 + \tau^4 + \mathcal{O}(\tau^6)], \end{aligned} \quad (25)$$

where we used the representation of the polylogarithm in terms of the Bernoulli polynomials [38, 24.8.3]

$$\text{Li}_n(e^{2\pi i z}) + (-1)^n \text{Li}_n(e^{-2\pi i z}) = -\frac{(2\pi i)^n}{n!} B_n(z). \quad (26)$$

In the limit  $\delta = \pi/2$ , our result agrees with the one in [39].

The range of validity of our result can be tested by comparing the low-temperature expansion with the numerically evaluated Matsubara sum. Fig. 2 shows the numerically calculated temperature corrections represented by dots and the asymptotic expansion (25) represented by lines as function of the effective temperature  $\tau = 2\pi L/\lambda_T$  and for different values of  $\delta$ . With decreasing temperature, the asymptotic expansion converges towards the numerically exact results as expected.

Already the results displayed in Fig. 2 indicate that  $\delta_{\text{crit}}$  depends on temperature. In fact, the low-temperature corrections for  $\delta = \delta_{\text{crit}}^{T=0}$  (filled squares) become positive for non-vanishing temperatures, suggesting that the value of the critical angle decreases with increasing temperature. This expectation is further corroborated by the high-temperature limit of the free energy in

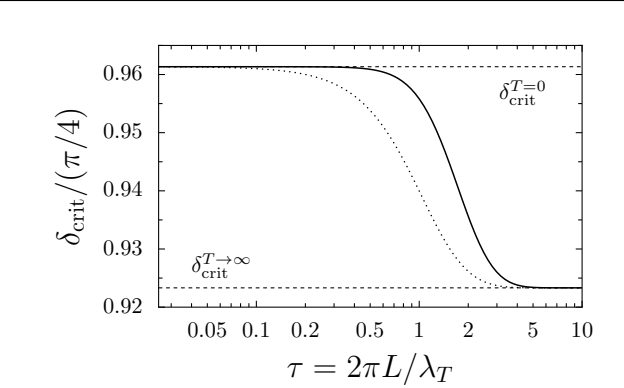


FIG. 3. The temperature dependence of  $\delta_{\text{crit}}$  in the PFA regime is shown by the solid line. For comparison, the value of  $\delta$  for which the free energy vanishes, is depicted by a dotted line. The dashed lines indicate the low-temperature value (23) and the high-temperature value (28) of the critical angle.

the PFA limit given by the first term in (24) as

$$\mathcal{F}_{T,\text{PFA}} = -\frac{k_B T}{4x} \text{Re} [\text{Li}_3(e^{2i\delta})] \quad (27)$$

which is in agreement with results found in the literature for  $\delta = 0$  and  $\delta = \pi/2$  [40, 41]. The high-temperature expression implies that the Casimir force vanishes at a critical value

$$\delta_{\text{crit}}^{T \rightarrow \infty} = 0.923 \dots \frac{\pi}{4}, \quad (28)$$

i.e., at a value below the zero-temperature critical value (23).

A numerical evaluation of the temperature dependence of  $\delta_{\text{crit}}$  yields the solid line in Fig. 3 showing that  $\delta_{\text{crit}}$  decreases monotonically with increasing temperature from the zero-temperature value (23) to the high-temperature value (28). The dotted line indicates the value of  $\delta$  where Casimir free energy vanishes. As the expressions (22) and (27) for the Casimir free energy at zero temperature and high temperatures, respectively, factorize into contributions depending on  $L$  and  $\delta$  separately, the Casimir free energy and the Casimir force vanish at the same value of  $\delta$  in these two limits. This no longer holds at intermediate temperature, as can be seen from the low-temperature expansion (25) where the dimensionless temperature  $\tau$  introduces an additional dependence on  $L$ .

The results for the temperature dependence of  $\delta_{\text{crit}}$  displayed in Fig. 3 imply that if we choose a system which can be described by a parameter in between  $\delta_{\text{crit}}^{T=0}$  and  $\delta_{\text{crit}}^{T \rightarrow \infty}$ , the Casimir force in the PFA regime will change from attractive to repulsive with increasing temperature. The transition occurs at temperatures around

$k_B T \approx 0.2 \hbar c / L$ , which at room temperature corresponds to a distance of about  $L = 1.5 \mu\text{m}$ . The enhancement of Casimir repulsion due to thermal fluctuations was also predicted for systems with metallic-based metamaterials [42] or in magnetodielectric systems [43]. In these cases, the repulsion originates from the contribution of the zero-frequency TE modes.

### B. Geometrical corrections to PFA

Going beyond PFA at zero temperature involves taking the leading corrections of an asymptotic expansion of (15) for  $x = L/R_{\text{eff}} \ll 1$  into account. A detailed analysis can be found in [33] where the leading geometrical corrections  $\Delta\mathcal{E}_{\text{PFA}} = \mathcal{E} - \mathcal{E}_{\text{PFA}}$  are shown to read

$$\Delta\mathcal{E}_{\text{PFA}} \approx \frac{\hbar c}{720\pi L} \left[ 20(\pi^2 - 6\delta(\pi - \delta)) - \frac{1-3u}{3} (\pi^4 - 30\delta^2(\pi - \delta)^2) \right]. \quad (29)$$

The geometrical corrections depend on the parameter  $u$  introduced in (13) which takes values between 0 and 1/4 corresponding to the sphere-plane geometry and a setup of two equally-sized spheres, respectively. The  $u$ -dependence indicates that with increasing separation, curvature effects become more important.

In order to verify that the leading correction to the PFA result is correct, we compare it with exact numerical results, which was not done in Ref. 33. Fig. 4 depicts the numerically calculated geometrical corrections over the whole range of aspect ratios  $x$  for the sphere-plane geometry, *i.e.*,  $u = 0$ . The four data sets correspond to the values of  $\delta$  used in Fig. 2 ranging from  $\pi/5$  to  $\pi/2$  and indicated here by the same symbols. As expected, for small aspect ratios, the results converge towards the values given by (29) and depicted by solid lines. In contrast, for large aspect ratios, the results approach the dashed lines representing the energy for a dipole-plane setup as given below by (42) for  $\tilde{\tau} \rightarrow 0$ .

The geometrical corrections presented in Fig. 4 let us expect that the critical angle  $\delta_{\text{crit}}$  where the Casimir force changes its sign not only depends on the temperature but also on the aspect ratio. This dependence will be discussed in more detail in Sec. VIII by making use of the data presented in Fig. 8.

### V. LONG-RANGE ASYMPTOTICS

If the two objects are sufficiently far apart from each other, the exponential decay of the translation matrix element (14) implies that the main contribution to the free energy is given by the single-round-trip expression obtained from (8) by retaining only the term with  $r = 1$ . For  $L \gg R_{\text{eff}}$ , *i.e.*, for distances much larger than the radius of the smaller sphere, it is even sufficient to restrict

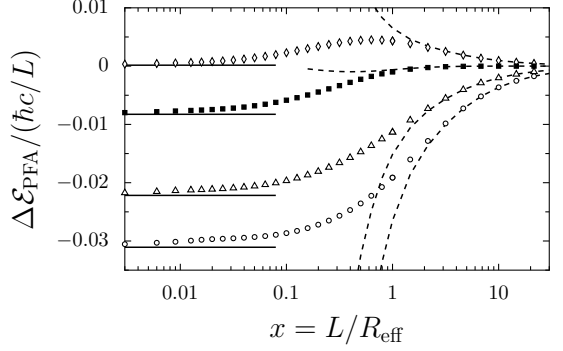


FIG. 4. Geometrical correction to the zero-temperature PFA result (22) for a sphere-plane setup, *i.e.*,  $u = 0$ , as a function of the aspect ratio (11) for the values of  $\delta$  used in Fig. 2 and indicated by the same symbols. The solid lines refer to the values obtained from (29) while the dashed lines represent the dipole-plane approximation (42) valid for large distances.

the single-round-trip result to the dipole contribution  $\ell = 1$ . Then, the trace over the round-trip operator in the multipole basis is given by

$$\text{tr}\mathcal{M} \approx \sum_{P=\text{E,M}} \sum_{m=-1}^1 \langle 1, m, P | \mathcal{M} | 1, m, P \rangle. \quad (30)$$

The evaluation of the coefficients depends on the geometry under examination. Both, the sphere-sphere and sphere-plane geometry have in common, that one object is given by a sphere. Separating the reflection operator of the sphere from the rest of the round-trip operator thus leads to

$$\langle m, P | \mathcal{M} | m, P \rangle = \sum_{P'=\text{E,M}} U_{P,P'}^{(m)} \langle m, P' | \mathcal{R}_1 | m, P \rangle \quad (31)$$

where, for simplicity, we drop the multipole moment from the states as in this section it always takes the value  $\ell = 1$ . Furthermore, we made use of the fact that the reflection matrix in the multipole basis is diagonal with respect to  $\ell$  and  $m$ .

The matrix elements of the reflection operator for a PEMC sphere are given by (2), where the reflection matrix (4) in the dipole limit yields

$$\mathbf{R}_{\text{PEMC}} \approx \frac{1}{6} \left( \frac{\xi R}{c} \right)^3 \begin{pmatrix} 1 + 3 \cos(2\theta_1) & 3 \sin(2\theta_1) \\ 3 \sin(2\theta_1) & 1 - 3 \cos(2\theta_1) \end{pmatrix}. \quad (32)$$

The matrix elements

$$U_{P,P'}^{(m)} = \langle m, P | \mathcal{T}_{12} \mathcal{R}_2 \mathcal{T}_{21} | m, P' \rangle \quad (33)$$

account for the translation operators and the remaining reflection operator in the multipole basis. In order to specify the matrix elements (33), we need to distinguish between the sphere-sphere and sphere-plane setup.

### A. Dipole-dipole limit

For two spheres with radii  $R_1, R_2$  much smaller than the surface-to-surface distance  $L$ , we can employ the dipole approximation also for the larger sphere. The matrix elements (33) can thus be written as

$$U_{P,P'}^{(m)} = \sum_{P'',P'''} \langle m, P | \mathcal{T}_{12} | m, P'' \rangle \langle m, P'' | \mathcal{R}_2 | m, P''' \rangle \times \langle m, P''' | \mathcal{T}_{21} | m, P' \rangle. \quad (34)$$

The eigenvalue  $m$  of the  $z$ -component of the angular momentum is conserved because the translations take place along the symmetry axis of the setup. The matrix elements for the reflection operator are defined in (32) and the matrix elements of the translation operator in the spherical-wave basis can be found in Eqs. (38)–(40) of Ref. 44.

After performing the sum over the Matsubara frequencies in (30), we obtain

$$\mathcal{F}_{\text{dip-dip}} = -\frac{\hbar c}{2\pi\mathcal{L}} \left( \frac{R_1 R_2}{\mathcal{L}^2} \right)^3 \left[ \cos^2(\delta) (f_{P,P}(\tilde{\tau}) + f_{P,\bar{P}}(\tilde{\tau})) - \sin^2(\delta) \left( \frac{4}{5} f_{P,P}(\tilde{\tau}) + \frac{5}{4} f_{P,\bar{P}}(\tilde{\tau}) \right) \right] \quad (35)$$

where  $f_{P,P}(\tilde{\tau})$  and  $f_{P,\bar{P}}(\tilde{\tau})$  are analytic functions of the effective temperature  $\tilde{\tau} = 2\pi\mathcal{L}/\lambda_T$  which account for channels conserving or changing polarization upon translation, respectively. Note that the dimensionless temperatures  $\tau$  and  $\tilde{\tau}$  use different distances  $L$  and  $\mathcal{L}$ , respectively. These functions can be found in Ref. 44 and are reproduced in (B1) for convenience. In the zero-temperature limit  $\tilde{\tau} \rightarrow 0$ , the Casimir energy is given by

$$\mathcal{E}_{\text{dip-dip}} = -\frac{\hbar c}{16\pi\mathcal{L}} \left( \frac{R_1 R_2}{\mathcal{L}^2} \right)^3 [8 + 135 \cos(2\delta)]. \quad (36)$$

For  $\delta = 0$  and  $\pi/2$  the expressions agree with the results obtained in Refs. 9 and 4, respectively.

In the previous section, it was already suspected that  $\delta_{\text{crit}}$  changes with the distance between the spheres. The upper bound for the critical angle in the zero-temperature limit can now be determined from (36) and yields

$$\delta_{\text{crit}}^{T=0} = \frac{1}{2} \arccos \left( -\frac{8}{135} \right) = 1.037 \dots \frac{\pi}{4}. \quad (37)$$

The critical angle, where the force vanishes, thus increases with distance as can be seen by comparing (37) with (23) for short separations. A more complete picture will be given in Fig. 8 and discussed in Sec. VIII.

In the high-temperature limit  $\tilde{\tau} \rightarrow \infty$ , the contribution of the polarization mixing channels  $f_{P,\bar{P}}$  vanishes and the free energy yields

$$\mathcal{F}_{T,\text{dip-dip}} = -\frac{3k_B T}{8} \left( \frac{R_1 R_2}{\mathcal{L}^2} \right)^3 [1 + 9 \cos(2\delta)] \quad (38)$$

which also agrees with a result in the literature for  $\delta = 0$  [9]. The magnetoelectric effect, responsible for the repulsion, reduces due to the vanishing polarization mixing channels. The critical angle is thus shifted towards a

larger value compared to the zero-temperature case

$$\delta_{\text{crit}}^{T \rightarrow \infty} = \frac{1}{2} \arccos \left( -\frac{1}{9} \right) = 1.070 \dots \frac{\pi}{4}. \quad (39)$$

Compared with the high-temperature result for short distances (28), one finds that the critical angle increases as the separation between the spheres grows. The distance dependence is thus similar to the one found in the low-temperature regime.

As can be seen from the solid line in Fig. 5, the critical angle  $\delta_{\text{crit}}$  increases monotonically with increasing temperature, which is consistent with the growth of  $\delta_{\text{crit}}$  with larger distances between the spheres. For systems with  $\delta$  in between the two limiting cases (37) and (39), the force changes from repulsion to attraction upon increasing the temperature. The transition occurs at temperatures  $k_B T \approx 0.8\hbar c/\mathcal{L}$ . The monotonic increase of  $\delta_{\text{crit}}$  with increasing temperature at large distances is in contrast to the opposite behavior found in the PFA regime as displayed in Fig. 3.

### B. Dipole-plane limit

Next, we consider the sphere-plane geometry for large distances. The reflection operator in (33) thus describes a PEMC plane. As the translation coefficients (14) are diagonal in the plane-wave basis, the matrix elements are conveniently expressed as

$$U_{P,P'}^{(m)} = \sum_{p,p'=\text{TE,TM}} \int \frac{d\mathbf{k}}{(2\pi)^2} e^{-2\kappa\mathcal{L}} \langle m, P | \mathbf{k}, p \rangle \times \langle \mathbf{k}, p | \mathcal{R}_2 | \mathbf{k}, p' \rangle \langle \mathbf{k}, p' | m, P' \rangle \quad (40)$$

with  $\mathcal{L} = L + R$ . PEMCs are idealized systems, where the reflection coefficients of a planar surface neither depend on the frequency nor on the incoming and outgoing wave vector. In the polarization subspace, the reflection

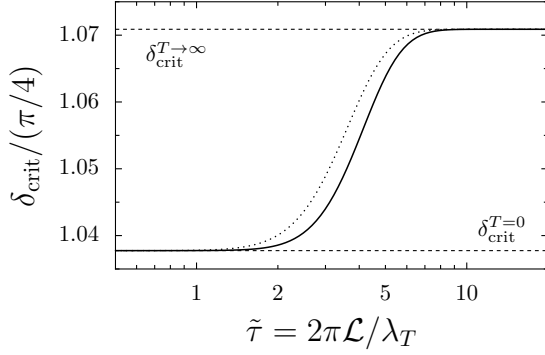


FIG. 5. The critical angle  $\delta_{\text{crit}}$  as function of the temperature is shown as solid line in the limit of large distance between the spheres. The dotted line refers to the values of  $\delta$  where the free energy changes its sign and the dashed lines indicate the low-temperature value (37) and high-temperature value (39) of the critical angle.

matrix elements for a plane characterized by the PEMC parameter  $\theta_2$  are thus given by [17, 45]

$$\langle p | \mathcal{R}_2 | p' \rangle = \begin{pmatrix} \cos(2\theta_2) & -\sin(2\theta_2) \\ -\sin(2\theta_2) & -\cos(2\theta_2) \end{pmatrix}. \quad (41)$$

Together with the basis transformation coefficients mentioned in connection with (16), the Casimir free energy can be calculated analytically and yields

$$\mathcal{F}_{\text{dip-plane}} = -\frac{\hbar c}{2\pi\mathcal{L}} \left(\frac{R}{\mathcal{L}}\right)^3 \cos(2\delta) [g_{P,P}(\tilde{\tau}) + g_{P,\bar{P}}(\tilde{\tau})]. \quad (42)$$

The functions  $g_{P,P}(\tilde{\tau})$  and  $g_{P,\bar{P}}(\tilde{\tau})$  account for the channels conserving and changing polarization during translation, respectively. They can be found in [44] and are reproduced in (B2) for convenience.

At zero temperature, the functions  $g_{P,P}$  and  $g_{P,\bar{P}}$  are given by the numerical factors 15/16 and 3/16, respectively. In the special case  $\delta = 0$ , our result thus agrees

with the one obtained in Ref. 46. In Fig. 4, the dipole-plane result (42) at zero temperature is depicted by the dashed lines for various values of  $\delta$ . In the high-temperature limit, the polarization-changing contribution  $g_{P,\bar{P}}$  vanishes while  $g_{P,P}$  yields  $3\tilde{\tau}/8$  which is in agreement with Ref. 47 for  $\delta = 0$ .

In the large-distance limit, the force changes its sign at the central angle, *i.e.*  $\delta_{\text{crit}} = \pi/4$ , for all temperatures. The critical angle only becomes dependent on temperature, if we take terms of the order of  $(R/\mathcal{L})^6$  and higher into account. These terms originate from higher multipole orders as well as from multiple scatterings between the objects.

## VI. HIGH-TEMPERATURE LIMIT

In the previous two sections, we have presented analytical results for small and large distances between the two objects. In order to gain a more complete understanding of the full range of distances, we consider the high-temperature limit, where analytical calculations of the Casimir interaction are possible. Recent studies [29, 33] showed that already the single-round-trip contribution provides useful insight into the Casimir interaction over the whole distance range between the objects. In the high-temperature limit (10), the single-round-trip expression

$$\mathcal{F}_T^{(1)} = -\frac{k_B T}{2} \text{tr} \mathcal{M}(0) \quad (43)$$

can be calculated analytically. By inserting the reflection matrix elements (18) into (15), we find that the trace can be expressed in terms of the traces of the round-trip operators for two PEC spheres ( $\delta = 0$ ) and the combination of a PEC and a PMC sphere ( $\delta = \pi/2$ ) as

$$\text{tr} \mathcal{M} = \cos^2(\delta) \text{tr} \mathcal{M}_{\text{PEC-PEC}} - \sin^2(\delta) \text{tr} \mathcal{M}_{\text{PEC-PMC}}. \quad (44)$$

The traces for the two limiting cases are given by

$$\begin{aligned} \text{tr} \mathcal{M}_{\text{PEC-PEC}} &= \frac{R_1 R_2}{\pi^2 \mathcal{L}^2} \int_0^1 dt \int_{-\infty}^{\infty} dx \int_{-\infty}^{\infty} dy e^{-(x_1^2 + x_2^2)} e^{-(y_1^2 + y_2^2)} \left[ (\cosh(\chi_{12}^{(1)}) - 1) (\cosh(\chi_{21}^{(2)}) - 1) \right. \\ &\quad \left. + (\cosh(\chi_{12}^{(1)}) - 2t_1 \cosh(t_1 \chi_{12}^{(1)})) (\cosh(\chi_{21}^{(2)}) - 2t_2 \cosh(t_2 \chi_{21}^{(2)})) \right] \end{aligned} \quad (45)$$

and

$$\begin{aligned} \text{tr} \mathcal{M}_{\text{PEC-PMC}} &= \frac{R_1 R_2}{\pi^2 \mathcal{L}^2} \int_0^1 dt \int_{-\infty}^{\infty} dx \int_{-\infty}^{\infty} dy e^{-(x_1^2 + x_2^2)} e^{-(y_1^2 + y_2^2)} \left[ (\cosh(\chi_{12}^{(1)}) - 1) (\cosh(\chi_{21}^{(2)}) - 2t_2 \cosh(t_2 \chi_{21}^{(2)})) \right. \\ &\quad \left. + (\cosh(\chi_{12}^{(1)}) - 2t_1 \cosh(t_1 \chi_{12}^{(1)})) (\cosh(\chi_{21}^{(2)}) - 1) \right]. \end{aligned} \quad (46)$$

Here, we performed a variable transformation  $(x_i, y_i) = \sqrt{k_i \mathcal{L}} (\cos(\varphi_i/2), \sin(\varphi_i/2))$  (see Ref. 48 for more details). The argument of the hyperbolic cosine reads  $\chi_{ij}^{(n)} = 2R_n(x_i x_j + y_i y_j)/\mathcal{L}$ . The integrals are of Gaussian type and can

be calculated by following the approach given in Ref. 49, which leads to

$$\text{tr}\mathcal{M}_{\text{PEC-PEC}} = \frac{y}{y^2 - 1} + \frac{1}{z} + \frac{z}{6} \log \left( \frac{z^2(y^2 - 1)}{(yz + 1/2)^2} \right) - \sum_{\sigma=\pm} \left[ \frac{1}{2y + \alpha_\sigma} - \frac{1}{6\sqrt{z}} \frac{1}{\alpha_\sigma^{3/2}} \log \left( \frac{2y^2 + \alpha_\sigma y - 1 + \sqrt{\alpha_\sigma z}}{2y^2 + \alpha_\sigma y - 1 - \sqrt{\alpha_\sigma z}} \right) \right] \quad (47)$$

and

$$\text{tr}\mathcal{M}_{\text{PEC-PMC}} = \frac{y}{y^2 - 1} + \frac{z - 2y}{2} \log \left( \frac{z^2(y^2 - 1)}{(yz + 1/2)^2} \right) - \sum_{\sigma=\pm} \left[ \frac{1}{2y + \alpha_\sigma} - \frac{1}{2\sqrt{z}} \frac{1}{\alpha_\sigma^{3/2}} \log \left( \frac{2y^2 + \alpha_\sigma y - 1 + \sqrt{\alpha_\sigma z}}{2y^2 + \alpha_\sigma y - 1 - \sqrt{\alpha_\sigma z}} \right) \right]. \quad (48)$$

In the high-temperature limit, the traces are only functions of the geometrical parameters of the system, with

$$y = \frac{\mathcal{L}^2 - R_1^2 - R_2^2}{2R_1 R_2} = 1 + x + \frac{u}{2}x^2, \quad (49)$$

where  $y$  is a conformally invariant distance scale. The parameters  $x$  and  $u$  were introduced in (11) and (13), respectively. Furthermore, we introduced

$$z = 2y + \alpha_+ + \alpha_- \quad (50)$$

with

$$\alpha_\pm = \frac{1 - 2u \pm \sqrt{1 - 4u}}{2u}. \quad (51)$$

The result for the sphere-plane geometry follows by taking the limit  $u = 0$  implying that  $\alpha_-$  vanishes while  $\alpha_+$  goes to infinity. The terms for  $\sigma = +$  in (47) and (48) thus yield zero. By summarizing the remaining terms one finds that the repulsive magnetoelectric term and the attractive term become identical in the sphere-plane limit and read

$$\begin{aligned} \text{tr}\mathcal{M}_{\text{PEC-PEC}}^{u=0} &= \text{tr}\mathcal{M}_{\text{PEC-PMC}}^{u=0} \\ &= \frac{y}{y^2 - 1} - \frac{1}{2y} + \frac{y}{2} \log \left( \frac{y^2 - 1}{y^2} \right). \end{aligned} \quad (52)$$

In Fig. 6, we compare the single-round-trip free energy scaled by the Apéry constant  $\zeta(3)$  with the exact high-temperature result for  $\delta = 0, \pi/6, \pi/3$ , and  $\pi/2$ . At large distances, the ratio approaches  $1/\zeta(3)$  thus confirming that the single-round-trip result becomes exact. At small distances, it differs from the exact result only by a factor of order one. In view of (10) and (20), the ratio at small distances is given by

$$\frac{\mathcal{F}_T}{\mathcal{F}_T^{(1)}} = \frac{\text{Re}[\text{Li}_3(e^{2i\delta})]}{\cos(2\delta)} \quad \text{for } x \ll 1. \quad (53)$$

The solid lines for  $u = 0$  and the dashed lines for  $u = 1/4$  for the same value of  $\delta$  barely differ, because the data are shown as a function of the conformally invariant distance scale  $y - 1$  which itself depends on  $u$ .

The monotonic behavior of the ratio  $\mathcal{F}_T/\mathcal{F}_T^{(1)}$  can be captured by a rational model [50]

$$\Phi_\delta = \prod_{k=1}^n \frac{e^{y-1} - 1 + \nu_k(\delta)}{e^{y-1} - 1 + \mu_k(\delta)} \quad (54)$$

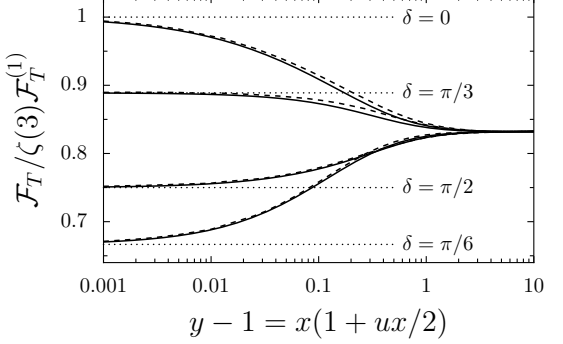


FIG. 6. Ratio of the high-temperature free energy  $\mathcal{F}_T$  and the single-round-trip result  $\mathcal{F}_T^{(1)}$  scaled by  $\zeta(3)$  as a function of the conformally invariant distance scale  $y - 1$  for different values of  $\delta$  and geometrical parameters  $u = 0$  (solid lines) and  $u = 1/4$  (dashed lines). The dotted lines represent the values  $1, 2/3, 8/9$ , and  $3/4$  for the ratio in the PFA limit corresponding to  $\delta = 0, \pi/6, \pi/3$ , and  $\pi/2$ , respectively.

TABLE I. Expansion coefficients for the rational model (54) fitting the ratio  $\mathcal{F}_T/\mathcal{F}_T^{(1)}$  for  $u = 0$  and  $u = 1/4$ . The last column shows the maximal relative deviation  $\Delta$  for all values of  $u$  and  $y$ .

$\delta$	$\nu_1$	$\nu_2$	$\mu_1$	$\mu_2$	$\Delta \times 10^3$
0	0.01148	0.18511	0.01103	0.16069	4.6
$\pi/6$	0.00020	0.07213	0.08928	0.00021	5.1
$\pi/3$	0.17655	0.25447	0.20505	0.20505	5.0
$\pi/2$	0.00468	0.21056	0.23221	0.00471	1.9

with the expansion coefficients obtained from a fit to the numerical results and given in Table I. The maximal relative deviation is of the order of a few per mill as indicated in the last column. The combination of the rational model with the single-round-trip result thus leads to a simple approximation of the free energy over the whole distance range. Note, that for the special case  $u = 0$  and  $\delta = \pi/4$  the single round-trip does not contribute. Then, the next order in the round-trip expansion (8) needs to be considered which will be discussed in the next section.

## VII. SUM RULE

Rode et al. [17] observed that the Casimir force between two parallel PEMC planes at zero temperature obeys the sum rule

$$\int_0^{\pi/2} d\delta F(\delta) = 0 \quad (55)$$

$$\int_0^{\pi/2} d\delta F(\delta) = -\frac{\hbar c}{32\mathcal{L}^2} \left( \frac{R_1 R_2}{\mathcal{L}^2} \right)^3 [18g(\tilde{\tau}) \cosh(\tilde{\tau}) + 18g(\tilde{\tau})^2 + 14g(\tilde{\tau})^3 \cosh(\tilde{\tau}) + 2g(\tilde{\tau})^4 (2 \cosh^2(\tilde{\tau}) + 1)] \quad (56)$$

with  $g(\tilde{\tau}) = \tilde{\tau} / \sinh(\tilde{\tau})$ . As a consequence, the sum rule is violated at zero temperature

$$\int_0^{\pi/2} d\delta F(\delta) = -\frac{7}{4} \hbar c \frac{(R_1 R_2)^3}{\mathcal{L}^8} \quad (57)$$

as well as in the high-temperature limit

$$\int_0^{\pi/2} d\delta F(\delta) = -\frac{9\pi}{8} k_B T \frac{(R_1 R_2)^3}{\mathcal{L}^7} \quad (58)$$

and for all temperatures in between.

The situation is different when one of the spheres is replaced by a plane. At small distances, the sum rule is still fulfilled like for the case of two spheres. However, from the dipole-plane result (42) one finds that the sum rule is also satisfied for large distances. Therefore, at large distances the transition from two spheres to a sphere in front of a plane is discontinuous.

In order to obtain a complete picture of the violation of the sum rule in the high-temperature limit, we present in Fig. 7 numerical results as a function of the distance for two equally sized spheres ( $u = 0.25$ , open triangles), for two spheres of considerably different size ( $u = 0.05$ , open diamonds and  $u = 0.01$ , open squares), and for a sphere and a plane ( $u = 0$ , filled circles). We scale the dimensionless integral over the thermal Casimir force

$$\mathcal{I} = \frac{\mathcal{L}}{k_B T} \int_0^{\pi/2} d\delta F_T(\delta) \quad (59)$$

by the geometrical factor  $y^3$  which reproduces the large-distance behavior of the Casimir force for both the sphere-plane and sphere-sphere setup. The value of the integral turns out to always possess a negative sign, implying that the enclosed area to the left of the critical angle, for which the force is attractive, is larger than the area to the right.

The lower panel of Fig. 7 shows how the violation of the sum rule increases from the PFA regime on the left to the

when integrated over the system parameter  $\delta$ . As the distance dependence factors out, the corresponding integral over the Casimir energy vanishes as well. A similar sum rule was found for the Casimir energy between a PEMC plate and a Weyl semimetal [51].

For two spheres, the sum rule can be expected to still hold in the PFA regime. At zero temperature, this can indeed be shown by integrating (22) over  $\delta$  while at finite temperatures one can make use of the series expansion of (20). More interesting is the large-distance limit. Starting from the dipole-dipole result (35), one finds

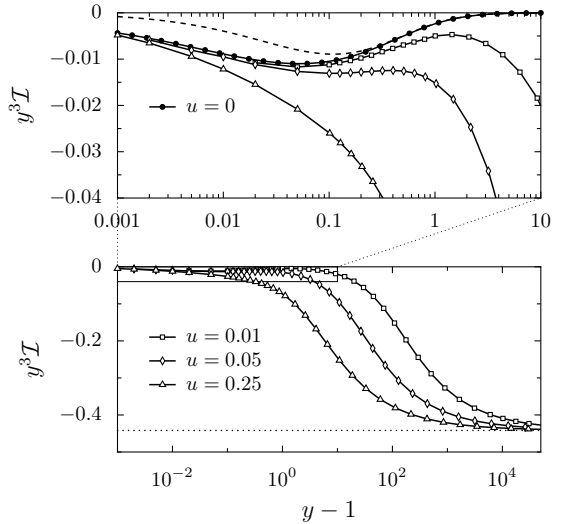


FIG. 7. Integral of the dimensionless Casimir force (59) in the high-temperature limit scaled by the geometrical factor  $y^3$ . The lower panel depicts the results for the sphere-sphere geometry with  $u = 0.25$  (open triangles),  $u = 0.05$  (open diamonds) and  $0.01$  (open squares). For large separations  $y - 1 \gg 1$ , the curves converge towards the dipole-dipole result  $-9\pi/64$  as indicated by the dotted line. The upper panel zooms into the upper left region of the lower panel and displays, in addition, the results for the sphere-plane setup ( $u = 0$ ) as filled circles. The dashed line corresponds to the values obtained from the double-round-trip approximation.

dipole-dipole regime on the right. At large distances, the scaled dimensionless integral approaches the asymptotic value  $-9\pi/64$  as indicated by the dotted line. The upper panel represents a zoom into the upper left region of the lower panel, allowing us to also present numerical data for the plane-sphere setup. Clearly, in this case the violation of the sum rule is significantly smaller than for the sphere-sphere setup.

The case of very different sphere radii is particularly interesting. We present data for  $u = 0.01$  and  $u = 0.05$ , which according to (13) for such small values is close to the ratio of the sphere radii. In the small distance regime, the violation of the sum rule is close to the one obtained for the plane-sphere setup. For intermediate distances, the violation starts to decrease before increasing again in order to approach the large-distance result. One thus observes a non-monotonic behavior of the scaled integral  $y^3 \mathcal{I}$ .

With the integral (59) for  $u = 0$  vanishing in the dipole-plane limit, an analytical description for the plane-sphere setup in the regime  $y \gtrsim 1$  requires to go beyond this limit and even beyond the single-round-trip approximation (44). Accounting for two round-trips, the trace over the square of the round-trip matrix yields

$$\begin{aligned} \text{tr} \mathcal{M}_{u=0}^2 &= \cos^2(2\delta) \text{tr} \mathcal{M}_{\text{PEC-PEC}}^2 \\ &\quad - \sin^2(2\delta) \text{tr} \mathcal{M}_{\text{PEC-PMC}}^2. \end{aligned} \quad (60)$$

The double-round-trip expression for the respective limiting cases of  $\delta = 0$  and  $\pi/2$  can be obtained from the single-round-trip results (47) and (48) for two spheres with the same radii [52] by replacing  $y$  by  $2y^2 - 1$ . The explicit expressions are given in Appendix C. As the two traces in (60) differ, the double-round-trip expression depicted by the dashed curve in the upper panel of Fig. 7 describes the leading violation of the sum rule at intermediate and large distances between sphere and plane.

### VIII. DISCUSSION

In the previous sections, we have examined the Casimir interaction for small and large distances as well as for low and high temperatures. The Casimir force was found to vanish for a critical material parameter  $\delta_{\text{crit}}$  which depends on the geometry and the temperature. In the following, we will discuss these results by focussing on the existence of an equilibrium position and its dependence on the temperature. While stable equilibrium positions were ruled out for reciprocal objects in vacuum [53], they are possible for non-reciprocal materials [29] as we shall see.

In Fig. 8, we show the curves of vanishing Casimir force as a function of the aspect ratio  $x$  and the material parameter  $\delta$  for the sphere-plane geometry ( $u = 0$ , solid lines) and two equally sized spheres ( $u = 1/4$ , dashed lines). The depicted curves delimit a region where curves for intermediate values of  $u$  can be found as is exemplified by the blue shaded area related to the case of zero temperature. The curves in Fig. 8 separate regions of repulsive Casimir force at smaller distances and attractive Casimir force at larger distances. They are therefore associated with stable equilibrium positions. For both geometries, blue and red curves depict the zero- and high-temperature limit, respectively. Curves for finite temperatures lie in between as indicated by the yellow shaded

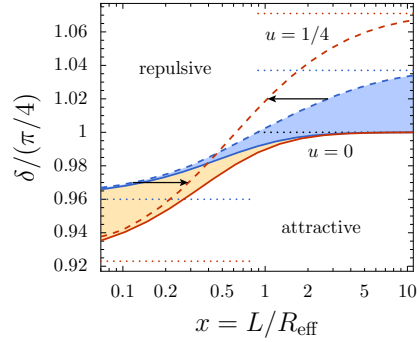


FIG. 8. Curves of vanishing Casimir force separating regions of attractive and repulsive force are shown as a function of the aspect ratio  $x$  and the material parameter  $\delta$ . Solid and dashed lines correspond to the sphere-plane geometry ( $u = 0$ ) and two equally sized spheres ( $u = 1/4$ ), respectively, while blue and red curves indicate the zero-temperature case and the high-temperature limit, respectively. The region covering all temperatures for  $u = 0$  is shaded in yellow while the region covering all aspect ratios in the zero-temperature limit are shaded in blue. The dotted lines indicate the asymptotic values for small and large distances. The arrows mark the opposite change of the equilibrium position with increasing temperature for  $u = 1/4$  for different values of  $\delta$ .

area for  $u = 0$ . All curves increase monotonically in  $\delta$  with increasing distance and converge towards the critical angles computed earlier and depicted by the dotted lines for small and large distances.

In our discussion of the PFA corrections in Sec. IV B, we observed that curvature effects become more important as the distance between the objects increases. The results presented in Fig. 8 confirm that the variation in the critical angle is smaller for a sphere in front of a plane as compared to two equally sized spheres. From a practical point of view, however, we are not so much interested in the effect of a variation of sphere radii which is difficult to realize, but rather in the effect of the more easily controllable temperature on the existence and variation of the equilibrium positions. The geometrical parameter  $u$  and the material parameter  $\delta$ , are thus fixed in the following.

We start with the sphere-plane geometry. According to the blue and red solid lines depicted in Fig. 8, the equilibrium distance increases with increasing temperature if  $0.96\pi/4 \lesssim \delta < \pi/4$ . Equilibrium positions do not exist for any temperature if the material parameter  $\delta$  exceeds  $\pi/4$ . In the regime  $0.92\pi/4 \lesssim \delta \lesssim 0.96\pi/4$ , the Casimir force can only vanish for not too low temperatures. A clearer picture of the temperature dependence can be obtained from Fig. 9, where the Casimir force relative to the Casimir force for two perfect reflectors ( $\delta = 0$ ) is shown as a function of the aspect ratio and the temperature. The chosen material parameters  $\delta = 0.95\pi/4$  and  $0.98\pi/4$  lie in the second and first range of material parameters, respectively, and correspond to two distinct scenarios. For the first value, an equilibrium

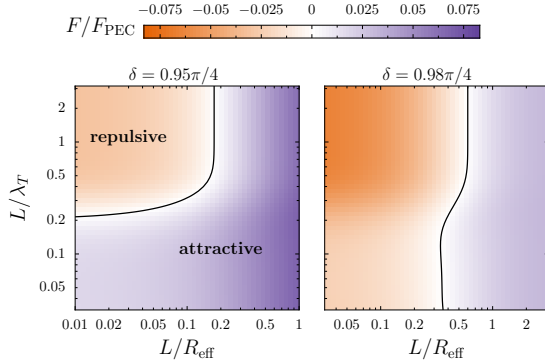


FIG. 9. Casimir force relative to the Casimir force for two perfect reflectors as a function of the effective distance and temperature for the sphere-plane geometry ( $u = 0$ ) with  $\delta = 0.95\pi/4$  (left) and  $0.98\pi/4$  (right). Negative (positive) values correspond to repulsion (attraction). The Casimir force vanishes along the solid line.

position only exists for temperatures above  $L/\lambda_T \approx 0.2$ . Below this threshold, the force is always attractive. For  $\delta = 0.98\pi/4$ , on the other hand, there exists an equilibrium distance for all temperatures, which increases until the high-temperature distance depicted by the solid red line in Fig. 8 is reached.

Turning to two equally-sized spheres ( $u = 1/4$ ), we first note that according to Fig. 8 there exists a critical material parameter of approximately  $0.99\pi/4$  where the equilibrium distance is independent of temperature. Below this value, the sphere-sphere geometry behaves qualitatively like the sphere-plane geometry discussed before. As the lower black arrow illustrates, the equilibrium distance is pushed to larger distances as temperature increases. The behavior changes for material parameters in the range  $0.99\pi/4 \lesssim \delta \lesssim 1.04\pi/4$ . There, the equilibrium distance decreases as the temperature increases, as indicated by the upper arrow and shown in Fig. 10 on the left for the specific material parameter  $\pi/4$ . For even larger values of  $\delta$  like for the case  $\delta = 1.05\pi/4$  shown in the right panel of Fig. 10, the Casimir force vanishes only for sufficiently large temperatures.

## IX. CONCLUSIONS

In this paper, we have extended the study of the Casimir interaction between perfect electromagnetic conductors to two spherical objects at finite temperatures. The Casimir interaction depends on a material parameter  $\delta$  which tunes the magneto-electric response and thus allows for a transition between an attractive and a repulsive Casimir force.

We found that the transition point  $\delta_{\text{crit}}$  depends on the geometric parameters as well as on temperature. For values of  $\delta$  around  $\pi/4$ , there exist sphere-sphere and sphere-plane setups where an equilibrium configuration is possible. The existence of equilibria requires the use

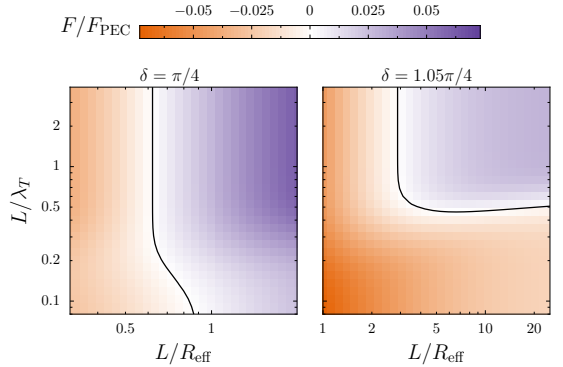


FIG. 10. Casimir force relative to the Casimir force for two equally-sized spheres ( $u = 1/4$ ) with  $\delta = \pi/4$  (left) and  $1.05\pi/4$  (right). Negative (positive) values correspond to repulsion (attraction). The Casimir force vanishes along the solid line.

of non-reciprocal materials to which PEMCs belong. For practical purposes, it is of particular interest that the equilibrium distance depends on the temperature, thus offering a scenario where the sign of the Casimir force can be controlled. Our theoretical study of the idealized system of perfect electromagnetic conductors may serve as a guide to explore more realistic materials for a geometry commonly employed in Casimir experiments.

## ACKNOWLEDGMENTS

The authors are grateful to Paulo A. Maia Neto, Serge Reynaud and Benjamin Spreng for insightful discussions.

## Appendix A: Scattering coefficients for a biisotropic sphere

We consider the scattering at a general biisotropic sphere of radii  $R$  in vacuum described by the matrix element

$$\langle \ell, m, P, \text{out} | \mathcal{R} | \ell', m', P', \text{reg} \rangle = -i^{P' - P} R_{P, P'} \delta_{\ell, \ell'} \delta_{m, m'} . \quad (\text{A1})$$

While the angular momentum variables  $\ell, \ell', m$ , and  $m'$  are conserved during the scattering process, this is not the case for the polarization. The coefficients  $R_{P, P'}$  account for the Mie coefficients as introduced in (2). The polarization-conserving scattering coefficients at imaginary frequencies  $\xi = -i\omega$  are given by

$$R_{\text{EE}}(i\xi) = C_\ell(\tilde{\xi}) \frac{W_\ell^R(\tilde{\xi}) A_\ell^L(\tilde{\xi}) + W_\ell^L(\tilde{\xi}) A_\ell^R(\tilde{\xi})}{V_\ell^R(\tilde{\xi}) W_\ell^L(\tilde{\xi}) + V_\ell^L(\tilde{\xi}) W_\ell^R(\tilde{\xi})} \quad (\text{A2})$$

$$R_{\text{MM}}(i\xi) = C_\ell(\tilde{\xi}) \frac{V_\ell^R(\tilde{\xi}) B_\ell^L(\tilde{\xi}) + V_\ell^L(\tilde{\xi}) B_\ell^R(\tilde{\xi})}{V_\ell^R(\tilde{\xi}) W_\ell^L(\tilde{\xi}) + V_\ell^L(\tilde{\xi}) W_\ell^R(\tilde{\xi})} \quad (\text{A3})$$

where we introduced for convenience

$$C_\ell(\tilde{\xi}) = (-1)^\ell \frac{\pi}{2} \frac{I_{\ell+1/2}(\tilde{\xi})}{K_{\ell+1/2}(\tilde{\xi})}. \quad (\text{A4})$$

Here,  $I_{\ell+1/2}(\tilde{\xi})$  and  $K_{\ell+1/2}(\tilde{\xi})$  are modified Bessel functions of first and second kind, respectively, of fractional order. The dimensionless frequency is given by

$$\tilde{\xi} = \frac{\xi R}{c}. \quad (\text{A5})$$

Moreover, we adopted the notation from Ref. 54 and defined the following auxiliary variables

$$\begin{aligned} A_\ell^{L,R}(\tilde{\xi}) &= \{I, \tilde{\xi}\} - m_{\mp}\{I, \tilde{\xi}m_{L,R}\} \\ B_\ell^{L,R}(\tilde{\xi}) &= m_{\mp}\{I, \tilde{\xi}\} - \{I, \tilde{\xi}m_{L,R}\} \\ V_\ell^{L,R}(\tilde{\xi}) &= m_{\mp}\{I, \tilde{\xi}m_{L,R}\} - \{K, \tilde{\xi}\} \\ W_\ell^{L,R}(\tilde{\xi}) &= \{I, \tilde{\xi}m_{L,R}\} - m_{\mp}\{K, \tilde{\xi}\} \end{aligned} \quad (\text{A6})$$

where following Ref. 55 we introduced the notation

$$\{\mathcal{I}, z\} = \frac{\mathcal{I}'_{\ell+1/2}(z)}{\mathcal{I}_{\ell+1/2}(z)} + \frac{1}{2z} \quad (\text{A7})$$

with  $\mathcal{I} = I, K$ . The relative refractive indices  $m_{L,R}$  for left- and right-polarized light are given by

$$m_{L,R} = \sqrt{\epsilon\mu - ((\beta + \alpha)/2)^2} \pm i(\beta - \alpha)/2. \quad (\text{A8})$$

The indices  $m_{\pm}$  account for the relative impedances

$$m_{\pm} = \frac{1}{\epsilon} \left[ \sqrt{\epsilon\mu - ((\beta + \alpha)/2)^2} \mp i(\beta + \alpha)/2 \right]. \quad (\text{A9})$$

It can easily be verified that the Mie coefficients for the electric and magnetic modes yield the known results in the isotropic limit, where  $\alpha = \beta = 0$ . The polarization mixing coefficients are defined as

$$\begin{aligned} R_{\text{ME}}(i\tilde{\xi}) &= iC_\ell(\tilde{\xi}) \left[ \{I, \tilde{\xi}\} - \{K, \tilde{\xi}\} \right] \\ &\times \frac{m_{-}\{I, \tilde{\xi}m_R\} - m_{+}\{I, \tilde{\xi}m_L\}}{V_\ell^R(\tilde{\xi})W_\ell^L(\tilde{\xi}) + V_\ell^L(\tilde{\xi})W_\ell^R(\tilde{\xi})} \end{aligned} \quad (\text{A10})$$

$$\begin{aligned} R_{\text{EM}}(i\tilde{\xi}) &= iC_\ell \left[ \{I, \tilde{\xi}\} - \{K, \tilde{\xi}\} \right] \\ &\times \frac{m_{-}\{I, \tilde{\xi}m_L\} - m_{+}\{I, \tilde{\xi}m_R\}}{V_\ell^R(\tilde{\xi})W_\ell^L(\tilde{\xi}) + V_\ell^L(\tilde{\xi})W_\ell^R(\tilde{\xi})}. \end{aligned} \quad (\text{A11})$$

In the PEMC limit, we find according to (3) that  $m_{L,R}$  goes to infinity while  $m_{\pm} = \mp i \tan(\theta)$  with  $\theta$  taking values between 0 and  $\pi/2$  accounting for a perfect electric and perfect magnetic conductor, respectively. The polarization conserving Mie coefficients thus yield

$$R_{\text{EE}} = -C_\ell \left[ \cos^2(\theta) \frac{\{I, \tilde{\xi}\}}{\{K, \tilde{\xi}\}} + \sin^2(\theta) \right] \quad (\text{A12})$$

$$R_{\text{MM}} = -C_\ell \left[ \cos^2(\theta) + \sin^2(\theta) \frac{\{I, \tilde{\xi}\}}{\{K, \tilde{\xi}\}} \right]. \quad (\text{A13})$$

The polarization-mixing coefficients are the same in the PEMC limit and they are given by

$$R_{\text{EM}} = R_{\text{ME}} = -C_\ell \left[ \frac{\{I, \tilde{\xi}\}}{\{K, \tilde{\xi}\}} - 1 \right] \frac{\sin(2\theta)}{2}. \quad (\text{A14})$$

It can now easily be shown that the Mie coefficients for a PEMC sphere can be obtained from the coefficients for a PEC by performing the transformation given in Eq. (4).

The reflection matrix elements in the plane-wave basis are expressed in terms of the amplitude scattering matrix (17). The scattering matrix connects an incident plane wave with a plane wave in the far-field of the object and is given by

$$S_{p,p'} = \sum_{\ell=1}^{\infty} \frac{2\ell+1}{\ell(\ell+1)} (R_{P,P'}\tau_\ell(z) + (-1)^{p-p'} R_{\bar{P},\bar{P}'}\pi_\ell(z)) \quad (\text{A15})$$

where we identify  $p = 1(2)$  with TM(TE) and  $P = 1(2)$  with E(M). The angular functions  $\tau_\ell(z)$  and  $\pi_\ell(z)$  defined in Ref. 54 depend on the in- and outgoing wave vectors

$$z = -\frac{c^2}{\xi^2} (kk' \cos(\varphi - \varphi') + \kappa\kappa'). \quad (\text{A16})$$

The term proportional to  $\pi_\ell$  can be neglected in the zero-frequency limit. The amplitude scattering matrix for a PEMC sphere can thus be expressed in terms of the scattering matrix for a PEC sphere

$$\mathbf{S}_{\text{PEMC}} = \mathbf{D}\mathbf{S}_{\text{PEC}}\mathbf{D}^{-1} \quad (\text{A17})$$

with the transformation matrix defined in (5). The matrix elements of the PEC scattering matrix are

$$\begin{aligned} (\mathbf{S}_{\text{PEC}})_{\text{TM,TM}} &= \frac{\xi R}{c} [\cosh(\chi) - 1] \\ (\mathbf{S}_{\text{PEC}})_{\text{TE,TE}} &= -\frac{\xi R}{c} \left[ \cosh(\chi) - 2 \int_0^1 t \cosh(t\chi) dt \right] \end{aligned} \quad (\text{A18})$$

where the argument of the hyperbolic cosine is defined as

$$\chi = 2R\sqrt{kk'} \cos\left(\frac{\varphi - \varphi'}{2}\right). \quad (\text{A19})$$

## Appendix B: Dipole limit

The Casimir free energy for large distances can be expressed in terms of dimensionless functions. For the sphere-sphere geometry the functions introduced in (35)

are given by

$$\begin{aligned}
f_{P,P}(\tilde{\tau}) &= \frac{5}{8} \left[ 6g(\tilde{\tau}) \cosh(\tilde{\tau}) + 6g^2(\tilde{\tau}) + 5g^3(\tilde{\tau}) \cosh(\tilde{\tau}) \right. \\
&\quad + g^4(\tilde{\tau})(1 + 2 \cosh^2(\tilde{\tau})) \\
&\quad \left. + g^5(\tilde{\tau}) \cosh(\tilde{\tau})(2 + \cosh^2(\tilde{\tau})) \right] \\
f_{P,\bar{P}}(\tilde{\tau}) &= \frac{1}{2} \left[ g^3(\tilde{\tau}) \cosh(\tilde{\tau}) + g^4(\tilde{\tau})(1 + 2 \cosh^2(\tilde{\tau})) \right. \\
&\quad \left. + g^5(\tilde{\tau}) \cosh(\tilde{\tau})(2 + \cosh^2(\tilde{\tau})) \right]
\end{aligned} \tag{B1}$$

where  $g(\tilde{\tau}) = \tilde{\tau}/\sinh(\tilde{\tau})$  with  $\tilde{\tau} = 2\pi\mathcal{L}/\lambda_T$ . The functions can also be obtained by combining Eqs. (42)–(46) in Ref. 44.

The large-distance behavior for the sphere-plane geometry (42) is characterized by the following functions

$$\begin{aligned} g_{P,P}(\tilde{\tau}) &= \frac{3}{16} [2g(\tilde{\tau}) \cosh(\tilde{\tau}) + 2g^2(\tilde{\tau}) + g^3(\tilde{\tau}) \cosh(\tilde{\tau})] \\ g_{P,\bar{P}}(\tilde{\tau}) &= \frac{3}{16} g^3(\tilde{\tau}) \cosh(\tilde{\tau}) \end{aligned} \quad (B2)$$

which can be found in Eqs. (20)–(22) of Ref. 44.

## Appendix C: Double round-trip in the high-temperature limit

In this appendix, we give the double-round-trip expression for the sphere-plane geometry in the high-temperature limit. The expression can be obtained from the single-round-trip result for two equally-sized spheres, due to the reflection symmetry of the two-sphere setup with respect to a plane perpendicular to the  $z$ -axis. The surface-to-surface distance between the spheres can as a result be seen as twice the distance for the sphere-plane geometry. Hence, after setting  $u = 1/4$  in (47) and (48) and replacing  $y$  with  $2y^2 - 1$ , we obtain the following double-round-trip expressions

$$\text{tr} \mathcal{M}_{\text{PEC-PEC}}^2 = \frac{2y^2 - 1}{4y^2(y^2 - 1)} + \frac{1}{4y^2} + \frac{2y^2}{3} \log \left( \frac{y^6(y^2 - 1)}{(y^2 - 1/4)^4} \right) - \frac{2}{4y^2 - 1} + \frac{1}{6y} \log \left( \frac{4y^3 - 3y + 1}{4y^3 - 3y - 1} \right) \quad (\text{C1})$$

$$\text{tr} \mathcal{M}_{\text{PEC-PMC}}^2 = \frac{2y^2 - 1}{4y^2(y^2 - 1)} + \log \left( \frac{y^6(y^2 - 1)}{(y^2 - 1/4)^4} \right) - \frac{2}{4y^2 - 1} + \frac{1}{2y} \log \left( \frac{4y^3 - 3y + 1}{4y^3 - 3y - 1} \right) \quad (\text{C2})$$

where  $y = 1 + L/R$  with the surface-to-surface distance  $L$  between a plane and a sphere with radius  $R$ .

- [1] F. M. Serry, D. Walliser, and G. J. Maclay, *J. Appl. Phys.* **84**, 2501–2506 (1998), URL <https://doi.org/10.1063/1.368410>.
- [2] I. E. Dzyaloshinskii, E. M. Lifshitz, and L. P. Pitaevskii, *Adv. Phys.* **10**, 165 (1961), URL <https://doi.org/10.1080/00018736100101281>.
- [3] J. Munday, F. Capasso, and V. A. Parsegian, *Nature* **457**, 170 (2009), URL <https://doi.org/10.1038/nature07610>.
- [4] T. H. Boyer, *Phys. Rev. A* **9**, 2078 (1974), URL <https://link.aps.org/doi/10.1103/PhysRevA.9.2078>.
- [5] V. Yannopapas and N. V. Vitanov, *Phys. Rev. Lett.* **103**, 120401 (2009), URL <https://link.aps.org/doi/10.1103/PhysRevLett.103.120401>.
- [6] R. Zhao, J. Zhou, T. Koschny, E. N. Economou, and C. M. Soukoulis, *Phys. Rev. Lett.* **103**, 103602 (2009), URL <https://link.aps.org/doi/10.1103/PhysRevLett.103.103602>.
- [7] A. G. Grushin and A. Cortijo, *Phys. Rev. Lett.* **106**, 020403 (2011), URL <https://link.aps.org/doi/10.1103/PhysRevLett.106.020403>.
- [8] A. G. Grushin, P. Rodriguez-Lopez, and A. Cortijo, *Phys. Rev. B* **84**, 045119 (2011), URL <https://link.aps.org/doi/10.1103/PhysRevB.84.045119>.
- [9] P. Rodriguez-Lopez, *Phys. Rev. B* **84**, 165409 (2011), URL <https://link.aps.org/doi/10.1103/PhysRevB.84.165409>.
- [10] W. Nie, R. Zeng, Y. Lan, and S. Zhu, *Phys. Rev. B* **88**, 085421 (2013), URL <https://link.aps.org/doi/10.1103/PhysRevB.88.085421>.
- [11] P. Rodriguez-Lopez and A. G. Grushin, *Phys. Rev. Lett.* **112**, 056804 (2014), URL <https://link.aps.org/doi/10.1103/PhysRevLett.112.056804>.
- [12] S. Fuchs, F. Lindel, R. V. Krems, G. W. Hanson, M. Antezza, and S. Y. Buhmann, *Phys. Rev. A* **96**, 062505 (2017), URL <https://link.aps.org/doi/10.1103/PhysRevA.96.062505>.
- [13] J. H. Wilson, A. A. Allocca, and V. Galitski, *Phys. Rev. B* **91**, 235115 (2015), URL <https://link.aps.org/doi/10.1103/PhysRevB.91.235115>.
- [14] Y. Ema, M. Hazumi, H. Iizuka, K. Mukaida, and K. Nakayama, *Phys. Rev. D* **108**, 016009 (2023), URL <https://link.aps.org/doi/10.1103/PhysRevD.108.016009>.

URL <https://link.aps.org/doi/10.1103/PhysRevD.108.016009>.

[15] V. K. Pappakrishnan, P. C. Mundru, and D. A. Genov, Phys. Rev. B **89**, 045430 (2014), URL <https://link.aps.org/doi/10.1103/PhysRevB.89.045430>.

[16] Z. Li and C. Khandekar, Phys. Rev. Appl. **16**, 044047 (2021), URL <https://link.aps.org/doi/10.1103/PhysRevApplied.16.044047>.

[17] S. Rode, R. Bennett, and S. Y. Buhmann, New J. Phys. **20**, 043024 (2018), URL <https://doi.org/10.1088/1367-2630/aaaa44>.

[18] A. H. Sihvola and I. V. Lindell, Microwave Opt. Technol. Lett. **4**, 295 (1991), URL <https://onlinelibrary.wiley.com/doi/abs/10.1002/mop.4650040805>.

[19] I. V. Lindell, A. H. Sihvola, S. Tretyakov, and A. Viitanen, *Electromagnetic waves in chiral and bi-isotropic media* (Artech House, Norwood, 1994), ISBN 978-0-89006-684-3.

[20] A. W. Rodriguez, A. P. McCauley, D. Woolf, F. Capasso, J. D. Joannopoulos, and S. G. Johnson, Phys. Rev. Lett. **104**, 160402 (2010), URL <https://link.aps.org/doi/10.1103/PhysRevLett.104.160402>.

[21] A. W. Rodriguez, D. Woolf, A. P. McCauley, F. Capasso, J. D. Joannopoulos, and S. G. Johnson, Phys. Rev. Lett. **105**, 060401 (2010), URL <https://link.aps.org/doi/10.1103/PhysRevLett.105.060401>.

[22] B. Spreng, P. A. Maia Neto, and G.-L. Ingold, J. Chem. Phys. **153**, 024115 (2020), URL <https://doi.org/10.1083/5.0011368>.

[23] C. F. Bohren, Chem. Phys. Lett. **29**, 458 (1974), URL <https://www.sciencedirect.com/science/article/pii/0009261474851444>.

[24] C. Caloz, A. Alù, S. Tretyakov, D. Sounas, K. Achouri, and Z.-L. Deck-Léger, Phys. Rev. Appl. **10**, 047001 (2018), URL <https://link.aps.org/doi/10.1103/PhysRevApplied.10.047001>.

[25] P. D. S. Silva, R. Casana, and M. M. Ferreira Jr., Phys. Rev. A **106**, 042205 (2022), URL <https://link.aps.org/doi/10.1103/PhysRevA.106.042205>.

[26] S. Y. Buhmann and S. Scheel, Phys. Rev. Lett. **102**, 140404 (2009), URL <https://link.aps.org/doi/10.1103/PhysRevLett.102.140404>.

[27] A. Lambrecht, P. A. Maia Neto, and S. Reynaud, New J. Phys. **8**, 243 (2006), URL <https://dx.doi.org/10.1088/1367-2630/8/10/243>.

[28] T. Emig, N. Graham, R. L. Jaffe, and M. Kardar, Phys. Rev. Lett. **99**, 170403 (2007), URL <https://link.aps.org/doi/10.1103/PhysRevLett.99.170403>.

[29] D. Gelbwaser-Klimovsky, N. Graham, M. Kardar, and M. Krüger, Phys. Rev. B **106**, 115106 (2022), URL <https://link.aps.org/doi/10.1103/PhysRevB.106.115106>.

[30] M. Nieto-Vesperinas, *Scattering and Diffraction in Physical Optics* (World Scientific, Singapore, 2006), ISBN 978-981-256-340-8.

[31] B. Spreng, M. Hartmann, V. Henning, P. A. Maia Neto, and G.-L. Ingold, Phys. Rev. A **97**, 062504 (2018), URL <https://link.aps.org/doi/10.1103/PhysRevA.97.062504>.

[32] R. Messina, P. A. Maia Neto, B. Guizal, and M. Antezza, Phys. Rev. A **92**, 062504 (2015), URL <https://link.aps.org/doi/10.1103/PhysRevA.92.062504>.

[33] T. Schoger, B. Spreng, G.-L. Ingold, and P. A. Maia Neto, Int. J. Mod. Phys. A **37**, 2241009 (2022).

[34] B. Derjaguin, Kolloid-Z. **69**, 155 (1934).

[35] O. Kenneth and I. Klich, Phys. Rev. Lett. **97**, 160401 (2006), URL <https://link.aps.org/doi/10.1103/PhysRevLett.97.160401>.

[36] M. Asorey and J. Muñoz-Castañeda, Nucl. Phys. B **874**, 852 (2013), ISSN 0550-3213, URL <https://www.sciencedirect.com/science/article/pii/S0550321313003301>.

[37] C.-J. Feng, X.-Z. Li, and X.-H. Zhai, Mod. Phys. Lett. A **29**, 1450004 (2014), URL <https://doi.org/10.1142/S0217732314500047>.

[38] DLMF, *NIST Digital Library of Mathematical Functions*, <http://dlmf.nist.gov/>, Release 1.1.4 of 2022-01-15, F. W. J. Olver, A. B. Olde Daalhuis, D. W. Lozier, B. I. Schneider, R. F. Boisvert, C. W. Clark, B. R. Miller, B. V. Saunders, H. S. Cohl, and M. A. McClain, eds., URL <http://dlmf.nist.gov/>.

[39] L. P. Teo, Phys. Rev. D **85**, 045027 (2012), URL <https://link.aps.org/doi/10.1103/PhysRevD.85.045027>.

[40] J. C. da Silva, A. Matos Neto, H. Q. Plácido, M. Revzen, and A. E. Santana, Physica A **292**, 411 (2001), URL <https://www.sciencedirect.com/science/article/pii/S0378437100005616>.

[41] S. C. Lim and L. P. Teo, New J. Phys. **11**, 013055 (2009), URL <https://doi.org/10.1088/1367-2630/11/1/013055>.

[42] F. S. S. Rosa, D. A. R. Dalvit, and P. W. Milonni, Phys. Rev. A **78**, 032117 (2008), URL <https://doi.org/10.1103/PhysRevA.78.032117>.

[43] C. Shelden, B. Spreng, and J. N. Munday, *Enhanced repulsive Casimir forces between gold and thin magnetodielectric plates* (2023), URL <https://doi.org/10.1103/PhysRevA.108.032817>.

[44] G.-L. Ingold, S. Umrath, M. Hartmann, R. Guérout, A. Lambrecht, S. Reynaud, and K. A. Milton, Phys. Rev. E **91**, 033203 (2015), URL <https://doi.org/10.1103/PhysRevE.91.033203>.

[45] I. V. Lindell and A. H. Sihvola, J. Electromagn. Waves Appl. **19**, 861 (2005).

[46] T. Emig, J. Stat. Mech. **2008**, P04007 (2008), URL <https://dx.doi.org/10.1088/1742-5468/2008/04/P04007>.

[47] A. Canaguier-Durand, P. A. Maia Neto, A. Lambrecht, and S. Reynaud, Phys. Rev. Lett. **104**, 040403 (2010), URL <https://link.aps.org/doi/10.1103/PhysRevLett.104.040403>.

[48] T. Schoger and G.-L. Ingold, SciPost Phys. Core **4**, 011 (2021), URL <https://scipost.org/10.21468/SciPostPhysCore.4.2.011>.

[49] T. Schoger, B. Spreng, G.-L. Ingold, A. Lambrecht, P. A. Maia Neto, and S. Reynaud, Int. J. Mod. Phys. A **37**, 2241005 (2022), URL <https://doi.org/10.1142/S0217751X22410056>.

[50] T. Schoger, B. Spreng, G.-L. Ingold, P. A. Maia Neto, and S. Reynaud, Phys. Rev. Lett. **128**, 230602 (2022), URL <https://doi.org/10.1103/PhysRevLett.128.230602>.

[51] T. Oosthuysse and D. Dудal, SciPost Phys. **15**, 213 (2023), URL <https://scipost.org/10.21468/SciPostPhys.15.5.213>.

[52] A. Bulgac, P. Magierski, and A. Wirzba, Phys. Rev. D **73**, 025007 (2006), URL <https://link.aps.org/doi/10.1103/PhysRevD.73.025007>.

[53] S. J. Rahi, M. Kardar, and T. Emig, Phys. Rev. Lett.

105, 070404 (2010), URL <https://doi.org/10.1103/PhysRevLett.105.070404>.

[54] C. F. Bohren and D. R. Huffman, *Absorption and Scattering of Light by Small Particles* (Wiley-VCH, Weinheim, 2004), ISBN 978-0-471-29340-8.

[55] H. M. Nussenzveig, *Diffraction Effects in Semiclassical Scattering* (Cambridge University Press, Cambridge, 1992), ISBN 978-0-521-38318-9.